Martensitic-like microstructures across the isostructural phase transitions in Cerium

Laura Henry, Nicolas Bruzy, Robin Fréville, Christophe Denoual, Bernard Amadon, Églantine Boulard, Andrew King, Nicolas Guignot, Agnès Dewaele

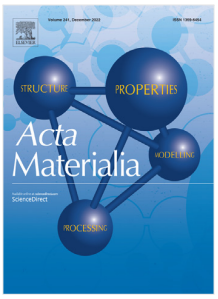

Martensitic-like microstructures across the isostructural phase transitions in Cerium

Laura Henry, Nicolas Bruzy, Robin Fréville, Christophe Denoual, Bernard Amadon, Églantine Boulard, Andrew King, Nicolas Guignot, Agnès Dewaele

PII: S1359-6454(24)00216-7
DOI: https://doi.org/10.1016/j.actamat.2024.119863
Reference: AM 119863

To appear in: *Acta Materialia*

Received date : 1 December 2023
Revised date : 28 February 2024
Accepted date : 21 March 2024

Please cite this article as: L. Henry, N. Bruzy, R. Fréville et al., Martensitic-like microstructures across the isostructural phase transitions in Cerium, *Acta Materialia* (2024), doi: https://doi.org/10.1016/j.actamat.2024.119863.

Martensitic-like microstructures across the isostructural phase transitions in Cerium

Laura Henry[1,2,3*], Nicolas Bruzy[1,2], Robin Fréville[1,2], Christophe Denoual[1,2], Bernard Amadon[1,2], Églantine Boulard[4], Andrew King[3], Nicolas Guignot[3], and Agnès Dewaele[1,2]

[1]CEA, DAM, DIF, F-91297 Arpajon, France
[2]Université Paris-Saclay, CEA, Laboratoire Matière en Conditions Extrêmes, F-91680 Bruyères-le-Châtel, France
[3]Synchrotron Soleil, F-91192 Saint Aubin, France
[4]Sorbonne Université, Muséum National d'Histoire Naturelle, UMR CNRS 7590, Institut de Minéralogie, de Physique des Matériaux et de Cosmochimie, IMPMC, F-75005 Paris, France
[*]laura.henry@synchrotron-soleil.fr

ABSTRACT

The isostructural gamma – alpha phase transition in elemental cerium is an electronic transition caused by a delocalization of the 4f electrons. This affects the bonding properties of Ce atoms and leads to a large volume collapse reaching ∼17% in the low pressure regime (< 2 GPa). While great attention has been drawn on the electronic description of this transition, attempts to understand the mesoscale mechanisms of this structural transition and their consequences in terms of microstructure remain scarce. We have investigated this transition by means of combined X-Ray Computed Tomography and Energy Dispersive X-Ray Diffraction on polycrystalline samples. Our experimental observations reveal a platelet-shape microstructure across the transition and up to the critical point, which have been associated to displacive mechanisms. Based on continuum mechanics modeling and ab initio calculations, we propose that here, this microstructure is initiated by elastic instability and shear anisotropy in the <100> directions.

Introduction

Rare Earth Cerium ([Xe] $4f^2\,6s^2$) may be one of the most intriguing elements with a unique phase transition under pressure. At ambient conditions of pressure and temperature, Cerium crystallizes in a face-centered cubic (fcc) phase also known as γ-Ce. At 295 K and 0.8 GPa, γ-Ce undergoes a first order phase transformation into α-Ce, another fcc structure with a density greater by ∼17%. The transition exhibits a hysteresis of around 3 kbar at 300 K but is completely reversible as the α phase is not recoverable at room conditions. α-Ce exhibits a greater thermal expansion coefficient than γ-Ce such that their volumes are equal at high temperature (600 K at 2 GPa[1]), and giving rise to a solid-solid critical point (SSCP) at 1.6 ± 0.1 GPa and 495 ± 15 K[2–4]. The existence of such a SSCP stands unique among all elements of the periodic table, making this transition even more fascinating.

Upon discovery of its isostructural character in 1949[5], this transition was regarded with great scientific interest as it suggested two enthalpy minima for the same structure. Two electronic scenarios have been proposed, Mott transition and Kondo Volume Collapse[6,7], which both describe $4f$ electrons as strongly correlated where γ-Ce and α-Ce bear localized and more delocalized $4f$ electrons, respectively. The two models differ in the origin of delocalization: the Mott and Kondo Volume Collapse models attribute it to ff and $f-spd$ hybridization, respectively. Athermal first principles methods based on DFT+DMFT or DFT+Gutzwiller[8–14] approximations now go beyond these models to describe more quantitatively the electronic structure at the transition. P-V-T, ultrasonic measurements[15–18] and *ab initio* calculations[10,13] described in details the thermodynamics of the $\gamma-\alpha$ transition. Experimental works evidenced its analogies with a Van der Waals liquid-gas transition such as the hysteresis and a bulk modulus softening approaching the first order transition below the SSCP, this softening being still observed in the homogeneous phase above it.

The mesoscopic mechanism of the transformation, and more particularly how two phases of very different volumes combine into an energy minimizing microstructure below SSCP, remains an enigma. Numerous displacive diffusionless transformations imply an undistorted invariant plane in the transition strain path[19]. This leads to a microscopically observable *habit plane*. This plane offers a low energy interface between parent and child phases, producing mixtures in the form of a lamellar microstructure following it, called martensitic microstructure. In the case of cerium, α and γ phase have the same structure with a different lattice parameter, which prevents the existence of such undistorted plane: the microstructure, in that sense, shall strongly differ

from usual strain-energy dominated martensitic transformations. Instead, one could expect a behavior similar to one observed in tin during the α-tin to β-tin transition at 286 K, accompanied by a large volume difference, that induces cracking and crumbling of the crystal and a complete loss of microstructure memory[20].

However, working with single crystal samples, Decremps *et al.*[15,16] evidenced a conservation of the crystalline orientation between parent γ and child α phases at different temperatures below SSCP. A dislocation-based massive plastic straining in combination with pure volume transformation, facilitated by the softening of the bulk modulus in γ-Ce, was proposed. This scenario of the transformation could not be confirmed in the absence of *in situ* observations[16]. *Ex situ* microscopy measurements made on samples partially and fully transformed to α, and recovered under γ form, evidence the formation of plastic strain bands along (111)[1] during the transformation. Zukas *et al.* showed that the amount of plastic deformation increases with the number of cycles of pressurization and with the fraction of sample transformed, varying pressure and temperature or pressure alone. These observations are consistent with lattice misorientations between γ-Ce and α-Ce up to 11° observed in single crystal XRD and interpreted by an array of edge dislocations[16]. Features of γ-α transformation have been measured for a polycrystalline porous Ce sample by X-ray tomography at 300 K, confirming the large volume decrease, however no monitoring of phase growth in γ-α coexistence domain has been attempted[21]. On the modeling side, the thermodynamics of the transition is correctly reproduced by a mean field approach with a system potential inspired by a Van der Waals fluid, and including a non-linear elasticity term to describe solid phases[22].

Here we report a combined synchrotron *in situ* X-ray tomography and X-ray diffraction study of both direct and reverse γ-Ce↔α-Ce transitions. We provide a fine monitoring of the three dimensional microstructures showing how α-Ce (γ-Ce) appears and coexists with the γ-Ce (α-Ce) parent phase. We show that despite the absence of any habit plane for these transformations, the transition microstructure has similarities with martensitic ones. Following earlier literature, we delved into the role of the elastic behavior of cerium on the transitions mechanism. *Ab initio* modeling was used to predict this behavior, where experimental data were missing. Then, a continuum model which uses these predictions is built to explain these surprising observations.

Experimental methods

Cerium samples were purchased from American Elements as poly-crystalline rods of 0.4 mm diameter and 1.5 mm in height. As received, the sample had witnessed partial surface oxidation that was removed by polishing under argon atmosphere to a size of 0.3 mm in diameter. Samples were loaded in Paris-Edinburgh assemblies, in contact with a hexagonal boron nitride (h-BN) capsule placed in a graphite furnace (see supplementary figure S2-1).

Energy-Dispersive X-Ray Diffraction (ED-XRD) and fast X-ray computed tomography (XCT) have been performed at the white beam station of the PSICHE beamline[23,24], using an Ultrafast Tomography Paris-Edinburgh Cell (UToPEc) press dedicated to tomographic measurements[25,26] (see supplementary figure S1-1).

In ED-XRD mode, a collimated incident beam of photons ranging from 15 - 100 keV is diffracted by the sample. A solid state detector collects the scattered light at an angle 2θ of 8° and around 1 m away from the sample and probes an azimuthal angle χ of 2.8° allowing qualitative texture observation. The volume probed is constrained by two pairs of slits located close to sample/detectors. Two modes of ED-XRD data collection are operated during the experiment: (i) at a fixed angle ω of the press or (ii) along 180° rotation ω of the press with integration over 3° (60 steps) or with finer steps of 1° (180 steps), referred to as polar ED-XRD hereafter. The first mode is used for metrology purpose (see Supplementary Materials) and the second mode allows orienting single crystal from the scattering signature of diffracting vertical planes and their concomitant angles.

XCT scans have been collected in pink beam mode, which offers a much greater flux than in a conventional monochromatic mode. A peak flux of about 76 keV has been used in order to optimize the imaging contrast and transmission for the highly absorbing Ce sample. Two-dimensional radiographic images with an effective pixel size of 0.65 μm have been collected during rotation of the press in the 0–180° range. Each tomographic reconstruction consists of 1500 frames that have been collected with an exposure time of 30 ms; the total time of acquisition is around a few minutes. The UToPEC offers a 165° angular opening which minimizes the missing angle reconstruction artefact arising from the two columns of the press.

Tomographic reconstructions, including phase and amplitude extraction following Paganin's method[27], have been performed based on the PyHST2 reconstruction software available at the PSICHE beamline and missing angle artefacts where corrected by iterative method simulating the forward projections, based on a grey level thresholding of the sample[28]. The true spatial resolution is 3.3 μm. Details of tomographic data treatment are presented in Supplementary S3.

During the experiments, pressure and temperature on the sample were remotely controlled through press oil pressure and resistive heating power. They were measured using power-temperature calibration and h-BN diffraction signal as detailed in Supplementary Material S2. ED-XRD was performed on selected volumes of the sample at same $P-T$ conditions as XCT, switching between the two modes taking a few minutes. Several experiments have been carried out, which allowed optimizing sample dimensions and shape, calibrations, data collection procedures and $P-T$ conditions.

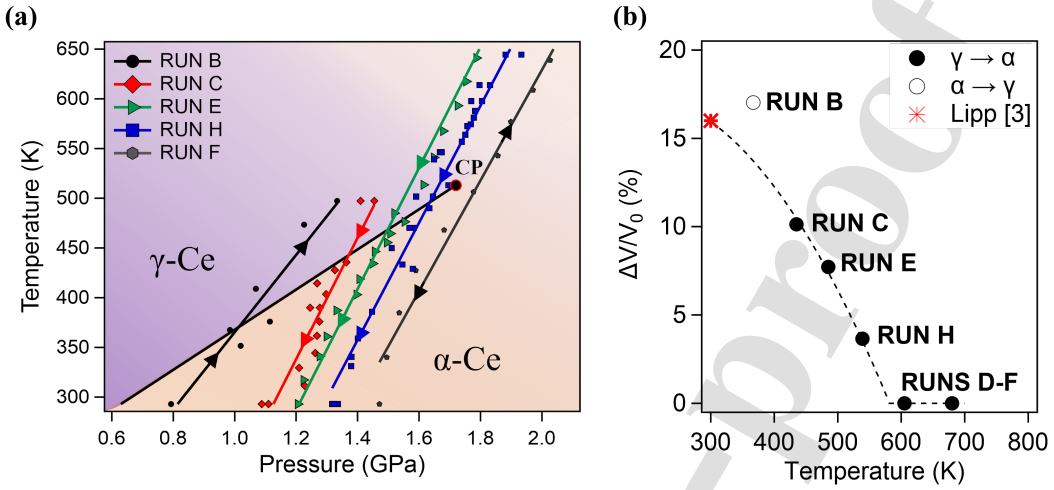

Figure 1. Thermodynamics of the transformation. (a) Phase diagram of Cerium in the region of interest[1]. The black solid line denotes the direct $\gamma \rightarrow \alpha$ transition line terminating on a critical point (denoted by the solid black/red circle). Pathways followed during this experiment are represented by the solid markers in selected colors to reflect the different runs that were performed. Arrows and lines are a guide to the eye.(b) Associated relative volume difference measured along the pathways shown in (a) as a function of the transition temperature. Run D is not represented in (a) but performed at pressures above the SSCP, similarly to run F.

The observations made during one experiment alone are reported below, but they have been confirmed by other runs, as reported in Supplementary Material S4. γ-Ce quasi-single crystals were synthesized and oriented on-line by high-temperature recrystallization. Then, the pressure-temperature paths represented in Figure 1 have been followed. It is the combination of XCT and XRD which allowed a quantitative understanding of Cerium isostructural transformation microstructures.

Experimental results

Synthesis of quasi-single crystal

In order to study *in situ* the microstructure produced at the transition, single crystals needed to be synthesized. Figure 2a shows XRD signal recorded for -as received- sample: all XRD peaks expected for fcc lattices are observed at all press angles ω and on the 7 pixels of the detector, evidencing its polycrystalline form. The temperature and pressure were slowly increased up to 800 K and 2.65 GPa in γ-Ce stability field in order to recrystallize Ce close to melting conditions. Temperature was limited to 800 K due to the high thermal conductivity of sintered diamond anvils used for their transparency in imaging experiments and pressure was increased to approach the melting curve minimum located at around 3 GPa and 950 K[29]. We have observed the progressive recrystallization from powder-like signal to multi-grains spotting formation and toward large grains with well-resolved and more intense Bragg reflections narrowed to only one vertical pixel of the detectors and spread to less than 6° in ω (with a resolution of 3°). However, at this stage (end of run B, Figure 2c), several single crystals coexisted and only one of them, which produced two XRD peaks in a sub-horizontal plane, could be oriented unambiguously. A second thermal recrystallization performed before run E produced a quasi-single crystal sample state with one principal grain orientation persisting over 450 microns in the height of the sample (Figure 2d and e).

Microstructures at the $\alpha \leftrightarrow \gamma$ transitions

After the synthesis of large single crystals in the sample, the critical point was circumvented to reach α-Ce stability field while preserving the sample microstructure. Then, $\alpha \rightarrow \gamma$ /$\gamma \rightarrow \alpha$ transitions were induced by temperature increase/decrease (run B/runs C and E) keeping the press load fixed. Runs D and F were conducted under super-critical conditions as shown in Figure 1.

The $\alpha \rightarrow \gamma$transition has been clearly identified in Run B from the onset of numerous platelets of lower density, initiated at 352 K (as shown in Figure 3), concomitant with observations made in ED-XRD showing the emergence of a new fcc phase with a volume larger by 17%, as expected at ∼1 GPa. Polar ED-XRD shows that new crystals of γ-Ce have close crystallographic orientations to starting α-Ce grains with a rotation of 3°, less than observed in reference[16]. Evolution of the microstructure at

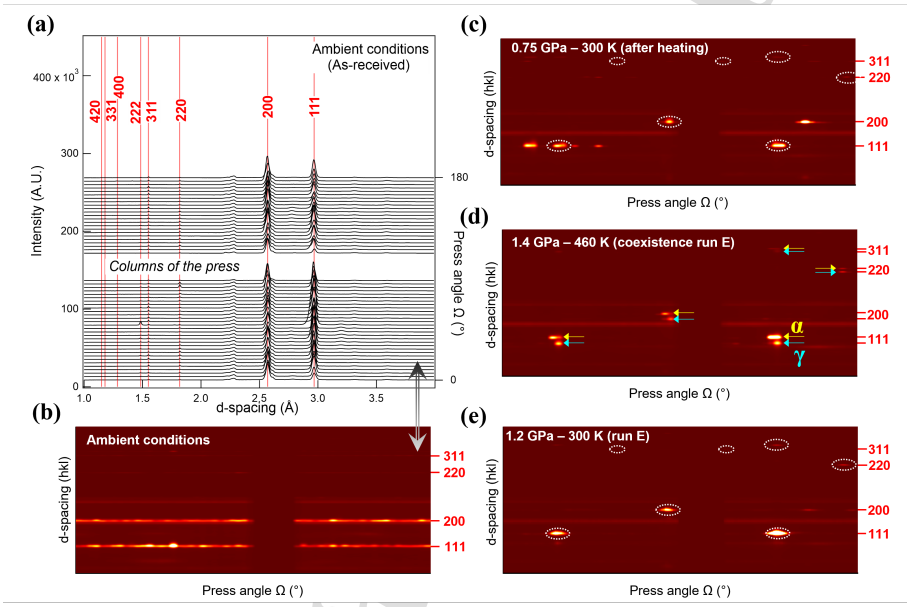

Figure 2. (a) Stacked graphs of cerium XRD signal obtained with 180° rotation of the press (angle ω) with 3° increments of the as-received sample at ambient conditions (b) corresponding cake representation (d-spacing (hkl) as a function of the press angle 0-180°). The continuous weak lines correspond to fluorescence lines of cerium. (c-d-e) Show the same acquisitions quenched from 800 K and 2.7 GPa (c), at the onset of the transition (d) and after run E (e). After the end of run B- (c), cake representation shows the emergence of strong preferred orientations which we interpret as the growth of single crystals from the initial polycrystalline sample. As the transition is cycled, one preferential orientation is preserved as witnessed in run E (denoted by the white dotted circle, belonging to the same orientation) (e). (d) Shows the coexistence of phases (yellow - α and cyan - γ). The orientation relationship shows the expected homothetic behavior with a mismatch in angle of ∼3°.

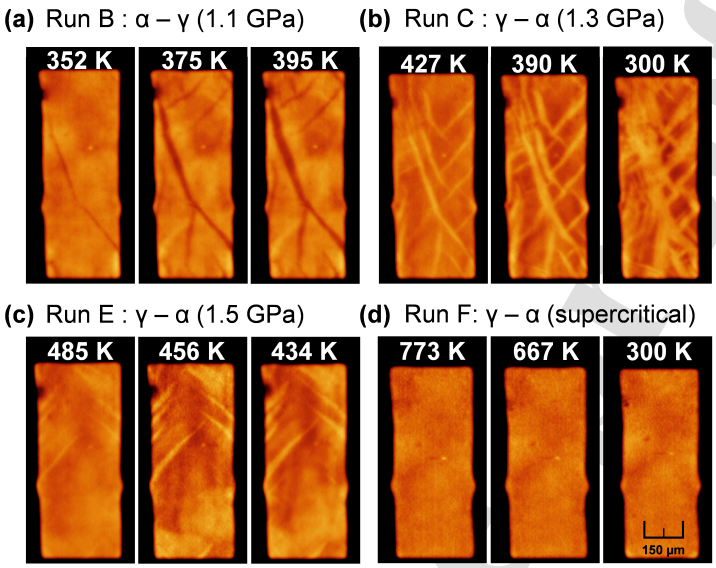

Figure 3. Selected slices of tomographic reconstructions collected along the four pathways of 1. Lighter colors indicate higher X-ray absorption. Continuous changes in colors can be due to reconstruction artefacts. (a) run B upon heating from α to γ at around 1.1 GPa associated with a volume increase of 18% at the transition. (b) run C on cooling from γ to α at 1.3 GPa associated with a volume decrease of -10% at the transition. (c) run E on cooling from γ to α at around 1.5 GPa associated with a volume decrease of -7% at the transition. (d) run F upon heating at 1.8 GPa above the SSCP where the transition occurs continuously between the two phases without coexistence.

transient stages of the transformation has been monitored with the collection of polar ED-XRD and tomography data every 10 K. The transformed microstructure consists in γ-Ce phase nucleated as platelets, which then grow through a homogeneous thickness increase, preserving their lenticular shape. Figure S5.1 (of the Supplementary Material) shows the thickness evolution of one platelet. The γ phase bursts as a 7 μm thick platelet at 352 K (where the imaging resolution limit is 3.3 μm due to the beamline geometry), increasing its thickness up to 50 μm at 500 K. Across the transition, furnace instabilities have resulted in a sudden increase in temperature as witnessed by the sudden increase in platelet thickness in the supplementary materials.

In Run C, the measured $\gamma \rightarrow \alpha$ volume difference is -10%. We observe that α-Ce platelets backward-nucleation reproduces the same microstructure as the forward one formed during run B, evidencing a memory effect of the microstructure (Figure 3). However, on the backward path (Run C), the α phase bursts as two distinct platelets of 10-15 μm thickness that grow toward each other to form the single larger platelet of 50 μm observed on the forward path (Run B). It suggests that those layers could be triggered by the presence of dislocations along the interfaces. For each run, the transition is completed through growth and coalescence of platelets.

Run E was performed after a second recrystallization at temperature above the critical point (run D) and offers the utmost single-crystallinity allowing for a quantitative analysis of the microstructure. At those conditions, the sample transformed from γ to α with a volume difference of -7% and the transition was witnessed again in the reconstructed volume with the appearance of numerous, thin (10 microns), platelets with a higher density concomitant with Bragg reflections belonging to the α phase. A cartography of the grain orientations performed at 300 K in the pure α phase as a function of the height of the sample revealed that a single orientation was dominant over 450 microns in height of the sample. Figure 4a shows the segmented microstructure at the coexistence of α and γ phases (P = 1.5 GPa and T = 456 K) where three dominant platelet orientations are clearly observed as indicated by the colored arrows. The 3D-Fourier transform of an XCT reconstruction is a good tool to quantitatively analyze microstructures, as shown in[26]. In particular, it allows evidencing preferred orientations in interfaces revealed with XCT. The stereographic projection of the 3D-Fourier transform of Figure 4a is represented in Figure 4b: it exhibits maxima close to the three directions of cerium crystallographic axes. These maxima, caused by the intensity variations due to the transformed platelets, are along the direction of normals to the platelets. The vertical platelets (indicated by black arrows in Figure 4a) thus have their normal roughly parallel to ± (010) directions in Ce single crystal; they are numerous and thicker and give rise to the highest maximum in the Fourier Transform. The wide extension of this peak results from the

lenticular or S-shape of the platelets. Platelets with (001) and (100) normals (light blue and green arrows in Figure 4a) are less numerous but still produce clear maxima in the Fourier transform. No other interfacial direction could be evidenced from the Fourier transform.

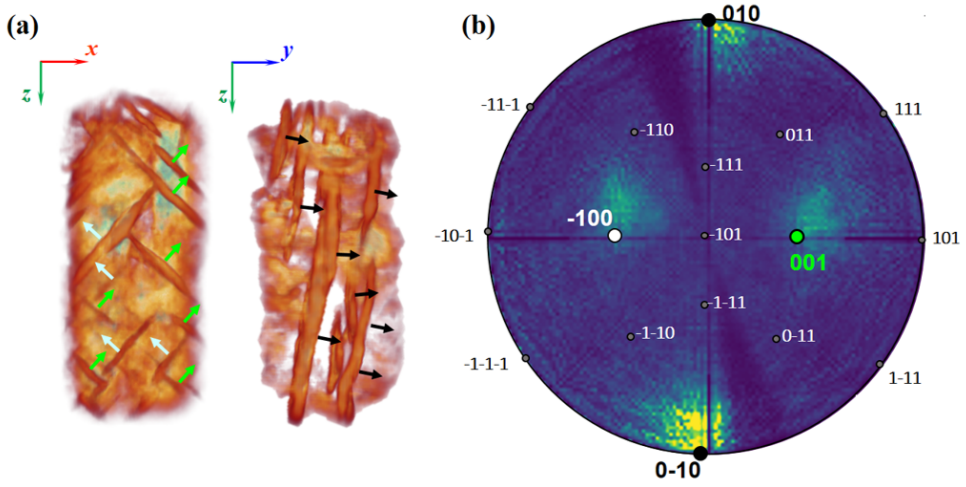

Figure 4. Analysis of γ → α transformation microstructure in run E. (a) Reconstructed volume of cerium at 1.5 GPa and 456 K, segmented to remove the lower intensity levels showing the α phase platelet. As the platelets are perpendicular to one another, projections are shown in Oxz and Oyz coordinate systems. (b) Superimposed stereographic projection of the γ-Ce crystal orientation determined from ED-XRD and stereographic projection of the modulus of the Fourier transform. The wavevector directions with Fourier transform maxima correspond to the normals to platelets. The three dominant orientations (with corresponding arrow colors) lie close to ±(010), (001) and (-100).

Critical point

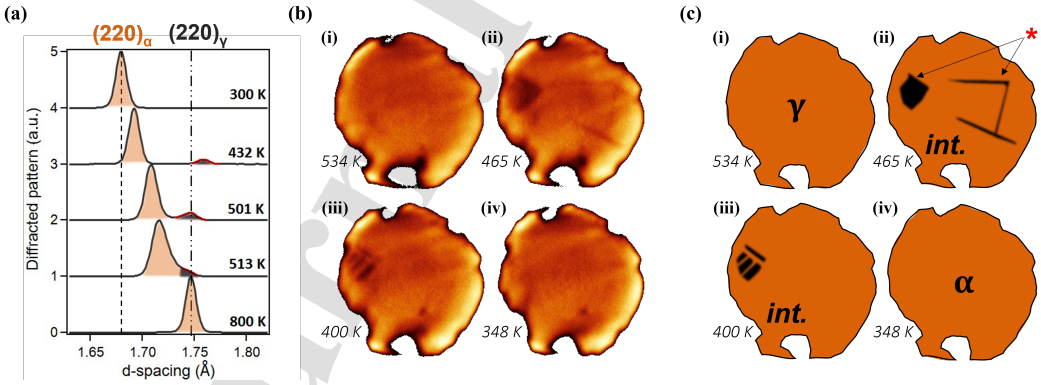

Figure 5. Transformation microstructure in the vicinity of the critical point. (a) ED diffracted patterns of Ce on the (220) reflection at selected temperatures between 800 K (γ-Ce) and 300 K (α-Ce). The sample continuously transforms into α-Ce until its volume become intermediary to both phases (539 K). At this temperature, we observe the appearance of γ-Ce (unstable at this conditions) that persists on further cooling. (b) Selected slices at different temperatures and (c) interpretation: (i) stability region of γ-Ce; (ii) intermediary (int.) region between α-Ce and γ-Ce, the darker grain and platelets corresponds to unstable γ-Ce (*). (iii) Metastable γ-Ce platelets disappear while α-Ce platelets form inside the metastable γ-Ce grain. (iv) The sample is fully α-Ce. (lighter regions are artefacts due to contrast saturation.

Run F was performed under supercritical conditions, and as expected no coexistence of phases with different densities has been observed (Figure 3d). An additional run was performed in conditions close to the SSCP (run H). In this run, the sample

was cooled from γ-Ce to α-Ce. Figure 5a shows the continuous shift of the (220) Bragg peak toward lower d-spacing (α -Ce), typical of a supercritical transformation. However, around 513 K, a faint peak corresponding to an unstable fcc phase with same orientation appears in addition to the major peak corresponding to an intermediary state between α- and γ-Ce. It manifests itself on the tomographic reconstruction as platelets and one grain of a lighter γ-Ce (dark brown) as seen in Figure 5c. At 430 K, γ-Ce platelets disappear while α-Ce platelets form and grow inside the γ-Ce grain until the sample fully converts to α-Ce. This unexpected behavior could be explained by inhomogeneous pressure drops within the sample as it is cooled, which would place the system just below the SSCP and induce locally a first-order phase transition.

To sum up, we have evaluated the microstructures produced for both the direct and reverse transitions, for different volume differences (18%, -10%, -7%), in the vicinity of the SSCP and above the SSCP, where the transition is continuous. Below the SSCP, where the transition is first order, the microstructures are surprisingly similar to martensitic ones, forming platelet-shaped child phase with the same orientation as the parent phase and an interface perpendicular to ⟨100⟩ directions. However, close to the critical point, when the transition volume is almost zero, the microstructure of the new phase can differ from platelets.

Discussion

Earlier attempts to describe the mesoscale mechanisms of the isostructural phase transition in cerium evidenced displacive features such as orientation relations[15,21]. Our study confirms this and reveals a microstructure akin to that obtained during martensitic transformations, in the form of a platelet-shaped child phase with the same orientation as the parent phase and an interface perpendicular to ⟨100⟩ directions. Similar microstructure is observed between 300K and 480K, for both the direct and reverse transitions, suggesting the temperature does not affect drastically the mesoscopic transitions mechanisms. The observed interface corresponds to a transformation strain minimum, as the habit plane in martensitic transformations[30]. However, the transition strain being a pure isotropic volume change, it should lead to an isotropic microstructure, e.g., fully disordered mix of parent and child phases. The question to answer is thus: what explains this anisotropic transformation microstructure?

Plasticity can be evoked as a possible source of anisotropy: the known plastic systems for fcc phases belong to (111) dense planes[31], consistently with observations of plastic deformation bands in cerium[32]. Plastic instabilities could thus produce a lamellar microstructure, but along (111) surfaces: this is not compatible with the observed (100) platelets. The role of the transformation strain and plastic deformation being excluded to explain the onset of (100) platelets, we evaluate below a possible role of an elastic instability on the mesoscopic transition mechanism, as mentioned for other first order solid-solid transitions[33,34]. One outstanding feature of the pressure effect on elastic response in γ -Ce is the softening of the bulk modulus reported by all experimental studies, up to the temperature conditions of the critical point[17,18,35,36]. In addition, a noticeable crystal elastic anisotropy has been measured in γ-Ce under ambient conditions[37,38]. Elastic anisotropy has been shown to affect conventional martensitic microstructures[39].

We investigate here whether elastic instability coupled with elastic anisotropy could be at play at the onset of a transformation to explain the emergence of platelets in absence of a habit plane. A continuum model of the γ-α transition is set below with a focus on the investigation of the tridimensional evolution of the microstructure. It is based on a form of the energy of the system similar to the mean field model by Bustingorry et al.[22] that describes the two phases with a different volume, including an elastic strain term. We go beyond this isotropic model and treat elastic energy with an elastic stiffness tensor including elastic anisotropy in both phases. This requires a precise knowledge of the values of the elastic stiffness tensors for both γ -Ce and α -Ce, which led us to perform *ab initio* computation of elastic coefficients in order to complement data available in the literature.

Single-crystal elastic constants of γ -Ce and α -Ce

At ambient conditions, the measured elastic constants of γ -Ce are C_{11} = 24.1 (26.01) GPa, C_{12} = 10.2 (14.26) GPa and C_{44} = 19.4 (17.3) GPa in[37] (and[38]). This denotes a noticeable crystal anisotropy yielding to a Zener ratio $Z = C_{44}/C' =$ 2.80 (2.95) for γ-Ce (with $C' = (C_{11} - C_{12})/2$ the second shear constant). C_{44} and C' correspond to a shearing along (100) and (110) planes, respectively (see below the corresponding strain tensors).

The effect of pressure on elastic anisotropy in γ -Ce has not been measured, owing to the unavailability of cerium single crystals under extreme conditions. However, under pressure, while the absolute values diverge, all experimental studies[17,18,35,36] report a softening of the bulk modulus as the pressure approaches the onset of the γ -α transition. In contrast, the average shear modulus increases by ∼35 % at the transition.

In α -Ce, only average shear moduli have been measured[17,18] which does not provide any constraint on the Zener ratio. The slopes of the transverse [110] branches of the phonon spectra of γ -Ce and α -Ce represented in reference[40] give only a hint that the Zener ratio is of the order of 3 in both phases.

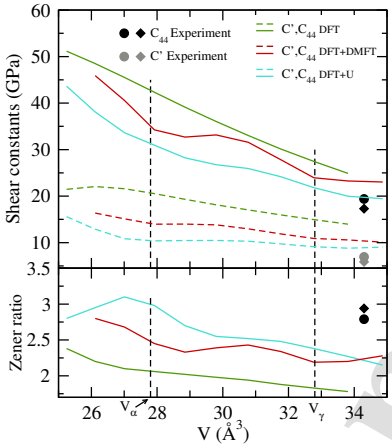

Figure 6. Shear elastic constants and Zener ratio computed in DFT, DFT+U and DFT+DMFT as a function of volume and compared to experiments (Ref. 37 (circle) and 38 (diamond)). The atomic volumes of the two phases at 0.8 GPa and 300 K are indicated by dashed vertical lines: 27.8 Å^3 and 32.8 Å^3, for of α -Ce and γ -Ce, respectively. Experiments[37,38] are performed at ambient pressure and thus for a higher volume (see e.g. Ref. 36).

To better constrain shear constants under pressure, and evaluate anisotropy, we perform first principles *ab initio* calculations, using three ab initio methods: Density Functional Theory (DFT), DFT+U and the combination of DFT with Dynamic Mean-Field Theory (DFT+DMFT)[41] in the ABINIT code[42–45]. These three methods involve different approximations of electronic interactions and predict equilibrium volume, equation of state, and electronic and magnetic properties of cerium[12,13,42,46], with varying success as detailed in Supplementary Materials alongside computational details. DFT + DMFT is considered as the most accurate for cerium, as it predicts the bulk modulus softening measured when compressing γ -Ce as well as the γ -α transition[12,13], in contrast to DFT and DFT+U.

Shear constants are computed for the three approximations using the finite difference method using the following strain tensors $\varepsilon(\delta)$ respectively for

$$C_{44} : \varepsilon(\delta) = \begin{pmatrix} 1 & \delta & 0 \\ \delta & 1 & 0 \\ 0 & 0 & \frac{1}{1-\delta^2} \end{pmatrix} \text{ and } C' : \varepsilon(\delta) = \begin{pmatrix} 1+\delta & 0 & \\ 0 & 1+\delta & 0 \\ 0 & 0 & \frac{1}{(1+\delta)^2}, \end{pmatrix} \quad (1)$$

The energy increase due to these two strains can be written as $E(\delta) - E(0) = 2VC_{44}\delta^2 + \mathcal{O}(\delta^3)$ and $E(\delta) - E(0) = 6VC'\delta^2 + \mathcal{O}(\delta^3)$. Computing E thus allows evaluating C_{44}, C' and Z. As discussed in the Supplementary Material, we use a value of 0.02 for δ.

The results are plotted in Figure 6. As expected, shear constants increase as volume decreases; they are larger with DFT than with DFT+DMFT and DFT+U. This is consistent with the fact that DFT and DFT+U respectively overestimates and underestimates bonding in cerium, whereas DFT+DMFT should provide a more trustful estimation. Interestingly, the three methods predict the same trend of shear constants vs. volume and a Zener ratio that mildly increases as volume decreases. DFT+DMFT Zener ratio is 2.2 at γ -Ce volume (experimental value of Z = 2.80-2.95) and 2.5 at α -Ce volume (at 0.8 GPa). These values could change depending on the parameters of the DFT+DMFT calculations (see Supplementary Materials). However, we can expect that the two extreme models of bonding, DFT and DFT+U, predict lower and upper bound values for the Zener ratio, which would then be predicted within ± 0.5.

Taking into account experimental values of Zener ratio in γ-Ce at 0 GPa and its variations predicted here ab initio, we consider that a value of Z=3 in γ-Ce and 3.5 in α-Ce are the most suited to describe elastic anisotropy in cerium.

Continuum mechanics modeling at the onset of the transition

The influence of elastic bulk instability and shear anisotropy in the nucleation of platelets is evaluated on the basis of the values computed above, in a continuum model described below. Since platelet formation has been evidenced at all tested temperatures during the experiments, no temperature dependence is assumed in the model as a first approximation. Simulations are then all based on parameters evaluated at 300K.

We propose an approximate of the free energy density Ψ_{tot} in cerium as a function of the elastic Green-Lagrange strain tensor E that has the exact (i.e. anisotropic) elasticity tensor for both γ-Ce and α-Ce, and that exhibits an unstable behavior for the in-between γ-αstates. More precisely, the transition is described under a finite strain continuum mechanics formalism using the Phase Field by Reaction Pathway (PFRP) framework[47]. A variation on the model formulated in reference[48] is proposed. In our model, the total free energy density of the system across the transition is:

$$\Psi_{tot} = \frac{1}{2} E : \underline{C}(V) : E + \Psi_{exc}(V). \tag{2}$$

It combines a quadratic elastic potential, where $\underline{C}$ is the material elasticity tensor based on elastic properties of both γ and α phases far from the transition, and Ψ_{exc} an excess energy that is defined such that the total free energy possesses the shape shown in Figure 7. Details on elasticity tensor $\underline{C}$ evaluation are given in Supplementary Material S7.

The total free energy has a negative second derivative (thus a negative bulk modulus) for volumes V/V_0 between ∼0.88 and ∼0.76, as indicated by the red lines in Figure 7. This range of volumes is prohibited, the system reaching a lower energy by splitting into γ-Ce and α-Ce, similarly to the volume-gas transition in a Van der Waals system. The energy profile can be modulated to adapt the prohibited volumes to the experimental volume change at a given temperature.

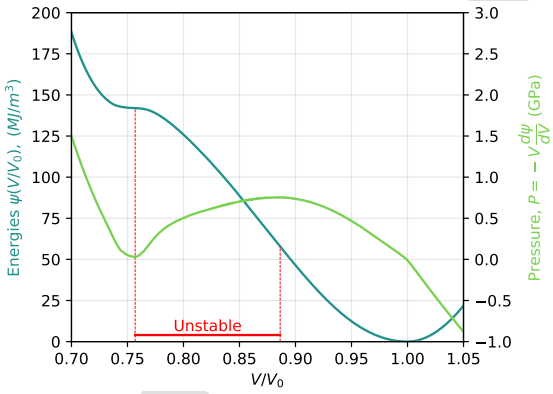

Figure 7. Total free energy Ψ_{tot} as a function of volume change, plotted from the energy outputs of PFRP calculations. Red lines delimit volumes for which the free energy has a negative second derivative, thus causing instability. Stability domains of γ-Ce and α-Ce phases can be identified at V/V_0=1.0 and V/V_0=0.74 respectively.

This free energy has been introduced in a 3D Lagrangian code based on an Element-Free Galerkin (EFG) interpolation[49]. The code relies on an explicit time integration and has been used previously to simulate the formation of platelet microstructures[50]. Simulations consist in submitting a γ-Ce single crystal to a gradual reduction in volume reaching 15%. By construction, parent and child phases have identical crystal orientations, as measured experimentally. The lattice basis is tilted by 55 °around $[1,1,1]$ axis to limit the possible influence of periodic boundaries on the onset of platelets. 128x128x128 volume elements were used in the computations.

Two simulations were performed to evaluate the effect of elastic instability alone, and elastic instability plus elastic anisotropy. In the first simulation, phase elastic behaviors are purely isotropic (Z=1), albeit slightly different in the two phases. As long as the prescribed volume deformation stays in the domain of stability of the γ phase, the deformation of the single crystal is homogeneous. In the unstable region, above 12% volume reduction, the volume partitions into regions of high and low densities, which correspond to the α and γ phases respectively (see Figure 8a). A microstructure is formed: it exhibits a mixture of regions of starting γ-Ce and transformed α-Ce. However, no clear interface orientation emerges. A stereographic projection of the Fourier transform's magnitude is provided in Figure S8.1 of the Supplementary Materials to highlight this point.

In the second simulation, an anisotropic elasticity tensor is used: Z=3 / 3.5 in γ-Ce / α-Ce (see Supplementary Materials S7 for the complete description of the elasticity tensor). Figure 8b shows the microstructure of the sample after phase separation (15% volume compression). α-Ce develops in the form of intersecting platelets. The stereographic projection of the Fourier transform's magnitude for the predicted densities is shown in Figure 8c for the anisotropic simulation. The intensity extrema lie close to (100) directions, depicting lamellar microstructures with plane normals along (100) directions of the crystal.

There is a good qualitative agreement between observed microstructures and calculated one in the anisotropic case. They both exhibit platelets of the child phase with ∼(001) oriented surfaces. The elastic softening of the bulk modulus enables the

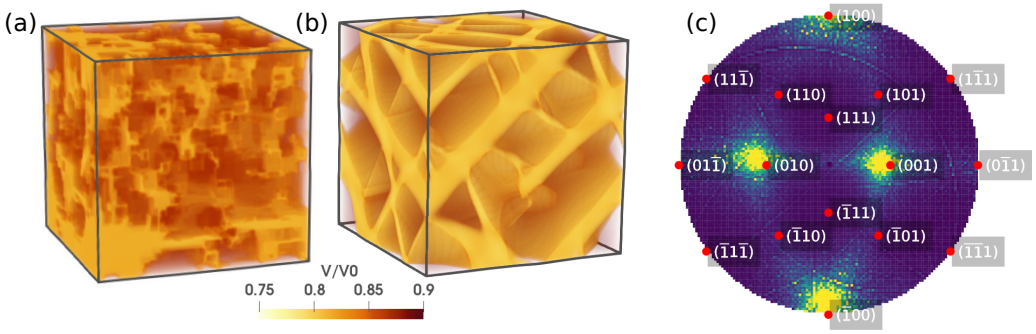

Figure 8. a) Mapping of the repartition of the local volume change $\frac{V}{V_0}$ at the onset of phase transformation during hydrostatic compression of a material with a Zener ratio value of 1 for both phases. Simulation is isothermal at 300K. **b)** Mapping of the repartition of the local volume change $\frac{V}{V_0}$ at the onset of phase transformation during hydrostatic compression of a material with Zener ratio values of ~ 3 and 3.5 for γ -Ce and α -Ce phases respectively. Simulation is isothermal at 300K. **c)** Pole figure projection, in the experimental γ -Ce crystal orientation, of individual direction intensities in Fourier space for the microstructure shown in b). Intensity maxima are colored in yellow.

phase segregation exhibited in Figures 8a and the shear anisotropy favors shearing along (110) planes. Indeed, shearing along (110) planes (C') cost three or 3.5 times less energy than shearing along (100) planes (C_{44}) in γ-Ce or α-Ce due to Z=3 or 3.5 in these phases. Here, the (100) interfaces seen in Figure 8b correspond to high strain gradients along (100) direction, which is equivalent to high shear strain along (110) directions: this is the orientation which is energetically favored due to shear anisotropy.

It should be noted that the von Mises (non-hydrostatic) stress calculated in α-Ce regions is high. This stress may be released by plastic activity, as observed experimentally[1]. This plastic activity is not included in the current model, which should thus describe only the onset of the transformation. Such feature could also account for the memory of platelets formation observed experimentally. The same platelets appearing in the same order for the direct and reverse transformation suggests that they can be triggered by the presence of dislocations or defects.

The current continuum model is a proof of concept that experimental lamellar microstructures could be induced by the combination of bulk softening, which induces strain localization, and shear anisotropy (with $C_{44}>C'$) which creates platelets with (100) normals. Although the interpretation of all experimental features of the transformation would require a more advanced model, it is worth noting that the volume change at the transition is set only by the shape of the free energy profile. The proposed mechanism is then likely to occur recurrently over the range of tested temperatures.

In summary, we used X-ray imaging techniques to reveal the microstructure emerging during the α-Ce–γ-Ce transition under extreme conditions, noticeably exhibiting platelets that would not be expected for this kind of transition. A simplified Lagrangian 3D large strain modeling of the transition demonstrates that elastic anisotropy coupled with bulk instability could explain the martensitic-like (platelet) microstructure observed. This required to improve the knowledge of elastic properties of cerium under pressure, e.g., by using DFT+DMFT estimations. It appears that the platelets microstructure is not formed due to an interface strain energy minimization process but to a free energy minimization process.

Data availability

The raw/processed data required to reproduce these findings cannot be shared at this time due to technical or time limitations.

References

1. Zukas, E., Pereyra, R. & Willis, J. The gamma to alpha phase transformation in cerium. *Metall. Transactions A* **18**, 35–42 (1987).
2. Young, D. A. *Phase diagrams of the elements* (Univ of California Press, 1991).
3. Koskenmaki, D. C. & Gschneidner Jr, K. A. Cerium. *Handb. on physics chemistry rare earths* **1**, 337–377 (1978).
4. Lipp, M. J. *et al.* Thermal signatures of the Kondo volume collapse in cerium. *Phys. Rev. Lett.* **101**, 165703, DOI: 10.1103/PhysRevLett.101.165703 (2008).

5. Lawson, A. & Tang, T.-Y. Concerning the high pressure allotropic modification of cerium. *Phys. Rev.* **76**, 301 (1949).
6. Johansson, B. The α-γ transition in cerium is a Mott transition. *The Philos. Mag. A J. Theor. Exp. Appl. Phys.* **30**, 469–482, DOI: 10.1080/14786439808206574 (1974).
7. Allen, J. W. & Martin, R. M. Kondo volume collapse and the $\gamma \rightarrow \alpha$ transition in cerium. *Phys. Rev. Lett.* **49**, 1106–1110, DOI: 10.1103/PhysRevLett.49.1106 (1982).
8. Held, K., McMahan, A. K. & Scalettar, R. T. Cerium volume collapse: Results from the merger of dynamical mean-field theory and local density approximation. *Phys. Rev. Lett.* **87**, 276404, DOI: 10.1103/PhysRevLett.87.276404 (2001).
9. Haule, K., Oudovenko, V., Savrasov, S. Y. & Kotliar, G. The $\alpha \rightarrow \gamma$ transition in Ce: A theoretical view from optical spectroscopy. *Phys. Rev. Lett.* **94**, 036401, DOI: 10.1103/PhysRevLett.94.036401 (2005).
10. Amadon, B., Biermann, S., Georges, A. & Aryasetiawan, F. The α- γ transition of cerium is entropy driven. *Phys. review letters* **96**, 066402 (2006).
11. Lanata, N. *et al.* γ- α isostructural transition in cerium. *Phys. review letters* **111**, 196801 (2013).
12. Bieder, J. & Amadon, B. Thermodynamics of the α-γ transition in cerium from first principles. *Phys. Rev. B* **89**, 195132, DOI: 10.1103/PhysRevB.89.195132 (2014).
13. Haule, K. & Birol, T. Free energy from stationary implementation of the DFT + DMFT functional. *Phys. Rev. Lett.* **115**, 256402, DOI: 10.1103/PhysRevLett.115.256402 (2015).
14. Amadon, B. & Gerossier, A. Comparative analysis of models for the $\alpha-\gamma$ phase transition in cerium: A DFT+DMFT study using Wannier orbitals. *Phys. Rev. B* **91**, 161103, DOI: 10.1103/PhysRevB.91.161103 (2015).
15. Decremps, F. *et al.* Diffusionless $\gamma \longleftrightarrow \alpha$ phase transition in polycrystalline and single-crystal cerium. *Phys. Rev. Lett.* **106**, 065701 (2011).
16. Moore, K. *et al.* Watching a metal collapse: examining cerium's $\gamma \longleftrightarrow \alpha$ transformation using x-ray diffraction of compressed single and polycrystals. *Acta Materialia* **59**, 6007–6016 (2011).
17. Decremps, F., Antonangeli, D., Amadon, B. & Schmerber, G. Role of the lattice in the two-step evolution of γ-cerium under pressure. *Phys. Rev. B* **80**, 132103, DOI: 10.1103/PhysRevB.80.132103 (2009).
18. Lipp, M. J. *et al.* Anomalous elastic properties across the γ to α volume collapse in cerium. *Nat. Commun.* **8**, 1198, DOI: 10.1038/s41467-017-01411-9 (2017).
19. Nishiyama, Z. *Martensitic transformation* (Elsevier, 2012).
20. Ojima, K., Taneda, Y. & Takasaki, A. Direct observation of $\alpha \rightarrow \beta$ transformation in tin by transmission electron microscopy. *Phys. Status Solidi (a)* **139**, 139–144, DOI: 10.1002/pssa.2211390111 (1993).
21. Hou, Q. *et al.* High pressure x-ray nano-tomography and fractal microstructures in the Ce γ-α transition. *J. Appl. Phys.* **125**, 135902 (2019).
22. Bustingorry, S., Jagla, E. & Lorenzana, J. Thermodynamics of volume-collapse transitions in cerium and related compounds. *Acta Materialia* **53**, 5183–5188, DOI: 10.1016/j.actamat.2005.07.027 (2005).
23. King, A. *et al.* Tomography and imaging at the PSICHE beam line of the SOLEIL synchrotron. *Rev. Sci. Instruments* **87**, 093704 (2016).
24. King, A. *et al.* Combined angular and energy dispersive diffraction: optimized data acquisition, normalization and reduction. *J. Appl. Crystallogr.* **55** (2022).
25. Boulard, E. *et al.* High-speed tomography under extreme conditions at the PSICHE beamline of the SOLEIL synchrotron. *J. Synchrotron Radiat.* **25**, 818–825 (2018).
26. Boulard, E. *et al.* Following the phase transitions of iron in 3d with x-ray tomography and diffraction under extreme conditions. *Acta Materialia* **192**, 30–39 (2020).
27. Paganin, D., Mayo, S. C., Gureyev, T. E., Miller, P. R. & Wilkins, S. W. Simultaneous phase and amplitude extraction from a single defocused image of a homogeneous object. *J. microscopy* **206**, 33–40 (2002).
28. Piault, P. *et al.* A thresholding based iterative reconstruction method for limited-angle tomography data. *Tomogr. Mater. Struct.* **2**, 100008 (2023).
29. Zhao, Y. & Holzapfel, W. Structural studies on the phase diagram of cerium. *J. alloys compounds* **246**, 216–219 (1997).
30. Ball, J. & Carstensen, C. Compatibility conditions for microstructures and the austenite–martensite transition. *Mater. Sci. Eng. A* **273-275**, 231–236, DOI: https://doi.org/10.1016/S0921-5093(99)00377-9 (1999).

31. Groves, G. W. & Kelly, A. Independent slip systems in crystals. *The Philos. Mag. A J. Theor. Exp. Appl. Phys.* **8**, 877–887, DOI: 10.1080/14786436308213843 (1963).

32. Zukas, E. G., Pereyra, R. A. & Willis, J. O. The gamma to alpha phase transformation in cerium. *Metall. Transactions A* **18**, 35–42, DOI: 10.1007/BF02646219 (1987).

33. Rehn, L. E., Okamoto, P. R., Pearson, J., Bhadra, R. & Grimsditch, M. Solid-state amorphization of zr_3al: Evidence of an elastic instability and first-order phase transformation. *Phys. Rev. Lett.* **59**, 2987–2990, DOI: 10.1103/PhysRevLett.59.2987 (1987).

34. Christian, J. W., Olson, G. B. & Cohen, M. Classification of displacive transformations : What is a martensitic transformation ? *J. Phys. IV France* **05**, C8–3–C8–10, DOI: 10.1051/jp4:1995801 (1995).

35. Voronov, F., Goncharova, V. & Stal'gorova, O. Elastic properties of cerium at pressures up to 84 kbar and at a temperature of 293 K. *Zh. Eksp. Teor. Fiz* **76**, 1351–1356 (1979).

36. Jeong, I.-K. *et al.* Role of the lattice in the $\gamma \rightarrow \alpha$ phase transition of Ce: a high-pressure neutron and x-ray diffraction study. *Phys. review letters* **92**, 105702 (2004).

37. Stassis, C., Gould, T., McMasters, O. D., Gschneidner, K. A. & Nicklow, R. M. Lattice and spin dynamics of γ-Ce. *Phys. Rev. B* **19**, 5746–5753, DOI: 10.1103/PhysRevB.19.5746 (1979).

38. Greiner, J., McMasters, O. & Smith, J. Single-crystal elastic constants of γ-cerium. *Scripta Metall.* **14**, 989–991, DOI: 10.1016/0036-9748(80)90372-5 (1980).

39. Tomida, T. Variant selection mechanism by elastic anisotropy and double ks relation for transformation texture in steel; difference between martensite and ferrite. *Acta Materialia* **146**, 25–41 (2018).

40. Krisch, M. *et al.* Phonons of the anomalous element cerium. *Proc. Natl. Acad. Sci.* **108**, 9342–9345, DOI: 10.1073/pnas.1015945108 (2011). https://www.pnas.org/doi/pdf/10.1073/pnas.1015945108.

41. Kotliar, G. *et al.* Electronic structure calculations with dynamical mean-field theory. *Rev. Mod. Phys.* **78**, 865–951, DOI: 10.1103/RevModPhys.78.865 (2006).

42. Amadon, B., Jollet, F. & Torrent, M. γ and β cerium: LDA$+U$ calculations of ground-state parameters. *Phys. Rev. B* **77**, 155104, DOI: 10.1103/PhysRevB.77.155104 (2008).

43. Amadon, B. *et al.* Plane-wave based electronic structure calculations for correlated materials using dynamical mean-field theory and projected local orbitals. *Phys. Rev. B* **77**, 205112, DOI: 10.1103/PhysRevB.77.205112 (2008).

44. Amadon, B. A self-consistent DFT+DMFT scheme in the projector augmented wave method: applications to cerium, Ce2O3and Pu2O3 with the hubbard I solver and comparison to DFT+U. *J. Physics: Condens. Matter* **24**, 075604, DOI: 10.1088/0953-8984/24/7/075604 (2012).

45. Romero, A. H. *et al.* ABINIT: Overview and focus on selected capabilities. *J. Chem. Phys.* **152**, 124102, DOI: 10.1063/1.5144261 (2020).

46. Streltsov, S. V. *et al.* Magnetic susceptibility of cerium: An LDA+DMFT study. *Phys. Rev. B* **85**, 195109, DOI: 10.1103/PhysRevB.85.195109 (2012).

47. Denoual, C., Caucci, A. M., Soulard, L. & Pellegrini, Y.-P. Phase-field reaction-pathway kinetics of martensitic transformation in model Fe_3Ni alloy. *Phys. Rev. Lett.* **105**, 035703 (2010).

48. Lafourcade, P., Denoual, C. & Maillet, J.-B. Mesoscopic constitutive law with nonlinear elasticity and phase transformation for the twinning-buckling of tatb under dynamic loading. *Phys. Rev. Mater.* **3**, 053610, DOI: 10.1103/PhysRevMaterials.3.053610 (2019).

49. Belytschko, T., Gu, L. & Lu, Y. Y. Fracture and crack growth by element free galerkin methods. *Model. Simul. Mater. Sci. Eng.* **2**, 519, DOI: 10.1088/0965-0393/2/3A/007 (1994).

50. Denoual, C. & Vattré, A. A phase field approach with a reaction pathways-based potential to model reconstructive martensitic transformations with a large number of variants. *J. Mech. Phys. Solids* **90**, 91 – 107, DOI: 10.1016/j.jmps.2016.02.022 (2016).

51. Giovenco, E. *et al.* Quantitative 4d x-ray microtomography under extreme conditions: a case study on magma migration. *J. Synchrotron Radiat.* **28**, 1598–1609 (2021).

52. Le Godec, Y. *et al.* Compression and thermal expansion of rhombohedral boron nitride at high pressures and temperatures. *J. Phys. Chem. Solids* **61**, 1935–1938 (2000).

53. Morard, G. *et al.* Optimization of paris–edinburgh press cell assemblies for in situ monochromatic x-ray diffraction and x-ray absorption. *High Press. Res.* **27**, 223–233 (2007).

54. Martin, A., Torrent, M. & Caracas, R. Projector augmented-wave formulation of response to strain and electric-field perturbation within density functional perturbation theory. *Phys. Rev. B* **99**, 094112, DOI: 10.1103/PhysRevB.99.094112 (2019).

Acknowledgements

The authors acknowledge the SOLEIL synchrotron radiation facility for the allocation of beam time (proposals 20210549 and 20200658). LH thanks J-P Itié for discussions. The DFT+DMFT calculations have been done on CEA-HF supercomputer. The continuum modeling simulations have been done on the supercomputers of the TGCC computing facility.

Author contributions statement

A.D. proposed the research, L.H, R.F, E.B, N.B, N.G. and A.D. conducted the experiments, L.H. and A.K. analysed and processed the data. N.B. and C.D. performed the continuum modeling simulations. B.A. performed DMFT simulations. All authors reviewed the manuscript.

MECHANISM OF THE 1st ORDER ISOSTRUCTURAL PHASE TRANSITION IN CERIUM

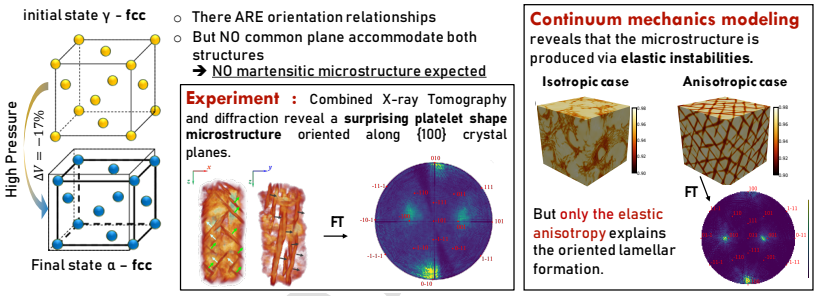

Declaration of interests

☒ The authors declare that they have no known competing financial interests or personal relationships that could have appeared to influence the work reported in this paper.

☐ The authors declare the following financial interests/personal relationships which may be considered as potential competing interests: